Precipitation Hardening of Mg-Zn and Mg-Zn-RE Alloys

L.Y. WEI, G.L. DUNLOP, and H. WESTENGEN

The age-hardening response of two cast Mg-Zn-RE alloys has been investigated and compared with that of a binary Mg-Zn alloy. The microstructures of the aged specimens were examined by analytical electron microscopy. Formation of a fine dispersion of rodlike β_1' precipitates is the main cause for age hardening, while extensive precipitation of disc-shaped β_2' coincides with the onset of overaging. Rare earth additions retard the formation of β_2' precipitates and thus postpone overaging. Four different orientation relationships between β_2' precipitates and matrix were found and explained in terms of the near-CSL model.

I. INTRODUCTION

A number of commercial magnesium casting alloys are based on the Mg-Zn binary alloy system[1] with small additions of rare earth elements. The rare earth additions, usually made by adding misch metal (MM) are known to improve the casting characteristics and elevated temperature strength.[2] One example is the sand-casting alloy ZE41 (3.5 to 5.0 wt pct Zn, 0.75 to 1.75 wt pct MM, and 0.4 to 1.0 wt pct Zr), which was developed to meet the needs of medium strength applications and which has good castability.[3,4] Another alloy with good castability and creep strength, EZ33, has approximately equal amounts of rare earth elements and zinc.[5]

Mg-Zn alloys have a pronounced response to age hardening. Investigations of their age-hardening behavior have shown that the age-hardening results from the precipitation of a transition phase (β_1').[6–14]

In the present work, the microstructures and the age-hardening characteristics of permanent mold cast Mg-Zn-RE pseudoternary alloys have been studied and compared with those of a binary Mg-Zn alloy in order to examine the effects of rare earth additions on precipitation and aging characteristics of this kind of alloy. The rare earth additions were made in the form of MM, since commercially pure MM is significantly cheaper than individual rare earth elements.

II. EXPERIMENTAL

The following permanent mold cast alloys were investigated (wt pct): Mg-8Zn-1.5RE, Mg-4Zn-1.5RE, and Mg-9Zn. The rare earth additions were made using MM, which is a mixture of approximately (wt pct) 50Ce, 25La, 20Nd, and 3Pr.

Specimens were solution treated for 4 hours at 315 °C followed by water quenching. They were subsequently age hardened for various times at 200 °C. In order to avoid burning or severe oxidation, the specimens were embedded in MgO powder during these heat treatments.

L.Y. WEI, Senior Research Scientist, is with the Department of Engineering Materials, Luleå University of Technology, S 971 87 Luleå, Sweden, G.L. DUNLOP, Professor, Department of Mining and Metallurgical Engineering, and Director, CRC for Alloy and Solidification Technology (CAST), is with the University of Queensland, Z 4072 Australia. H. WESTENGEN, Section Manager, is with the Department of Magnesium Materials Technology, Norsk Hydro a. s., Research Centre Porsgrunn, N-3901 Porsgrunn, Norway.
Manuscript submitted August 24, 1994.

Both macro- and microhardness measurements were made on the age-hardened specimens. Specimens for scanning electron microscopy (SEM) were mechanically polished followed by etching with $1/3HNO_3$ in ethanol and investigated using a JEOL 733 SEM. Thin foils for transmission electron microscopy (TEM) were prepared by electropolishing in $1/3HNO_3$ in ethanol at 8 to 15 V and ~ 0 °C and subsequently ion beam thinning for about 1 hour with an incidence angle of ~ 15 deg in order to remove the oxide layer that formed during electropolishing. The thin foil specimens were then examined in a JEOL 2000 FX TEM/STEM instrument operating at 200 keV.

III. RESULTS

A. The General Microstructure of the Cast Specimens

The SEM micrographs in Figure 1 show the microstructures of the three as-cast alloys. All of the alloys had a dendritic cast structure with large intergranular precipitates present between the dendrites. The dendrites were essentially a magnesium-rich supersaturated solid solution. The microstructure of the Mg-Zn alloy was significantly coarser than that of the "ternary" alloys. The amount of coarse intergranular precipitates was considerably greater in the ternary alloy containing 8 pct Zn than that containing only 4 pct Zn. The intergranular microstructures of the cast Mg-9Zn and Mg-8Zn-1.5RE alloys have been described in considerable detail elsewhere.[15] The interdendritic phase in the as-cast Mg-9Zn alloy is $Mg_{51}Zn_{20}$, and this decomposed to $MgZn_2$ Laves phase and $\alpha(Mg)$ during solution treatment. In the Mg-8Zn-1.5RE alloy, the predominant intergranular phase is T phase, which forms in the temperature range 480 °C to 447 °C during solidification.[15,16] Other intergranular phases in this alloy were Mg_4Zn_7 and a pseudobinary $MgZn_2$ phase with a crystal structure similar to the $MgZn_2$ Laves phase. For the Mg-4Zn-1.5RE alloy, only T phase was found after solidification. None of the Mg-Zn binary intergranular phases formed in this alloy during solidification.

B. Age-Hardening Response

The macro- and microhardnesses of specimens that had been solution treated at 315 °C and age-hardened for different times at 200 °C are shown in Figure 2. For the two rare earth containing alloys, the general hardness

Fig. 2—Age-hardening response for binary and ternary alloys during aging at 200 °C: (a) macrohardness and (b) microhardness within the dendrites.
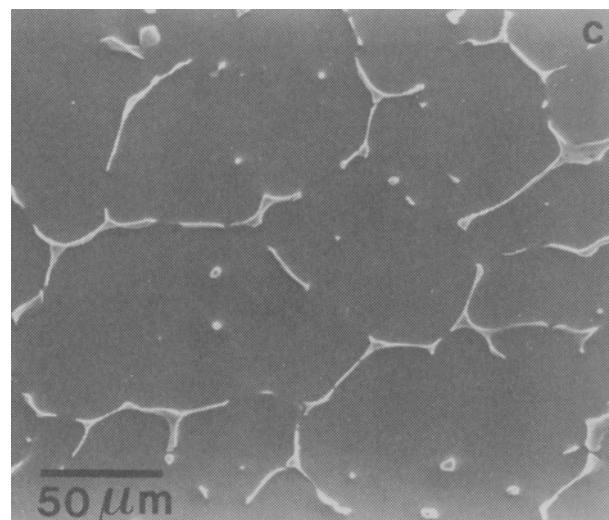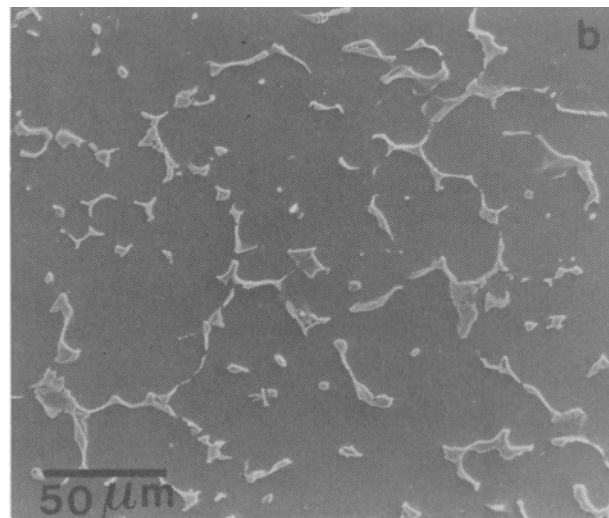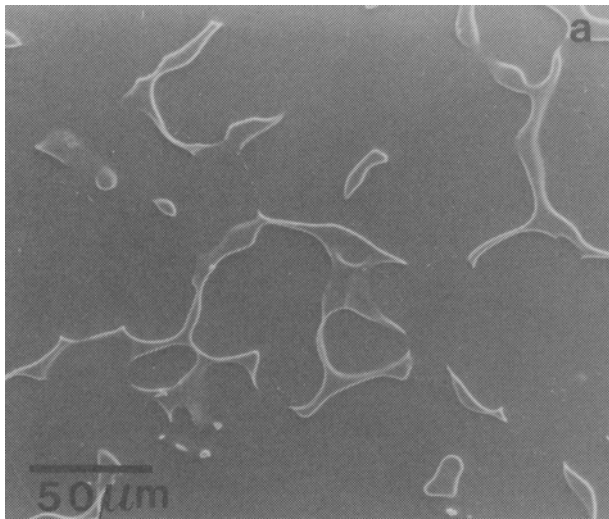
Fig. 1—Microstructures of the as-cast alloys (SEM): (a) Mg-9Zn, (b) Mg-8Zn-1.5RE, and (c) Mg-4Zn-1.5RE.
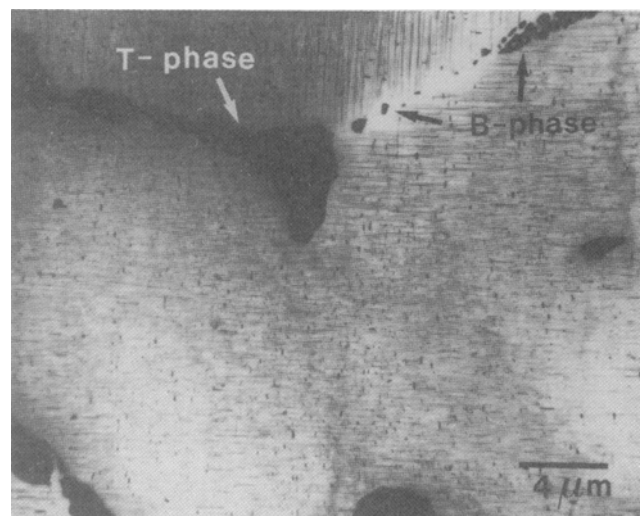
Fig. 3—General microstructure of Mg-8Zn-1.5RE alloy aged at 200 °C for 50 h (TEM).

level of the alloy containing 8 pct Zn was considerably greater than that of the alloy containing 4 pct Zn. This is to be expected because of the large amount of interdendritic second phases present in the 8 pct Zn alloy. The aging response of the two ternary alloys was however very similar with peak hardnesses occurring after about 20 hours aging. This can be seen more clearly from the microhardness values in Figure 2(b), where the hardness tests were made within the dendrites without interference from the coarse intergranular particles. It can be noted from the values of the microhardnesses that the aging peak occurred after about 10 hours aging for the Mg-Zn alloy and that this binary alloy overaged more rapidly than the two rare earth containing alloys.

C. *General Microstructure of the Age-Hardened Alloys Specimen*

A low-magnification TEM micrograph of the Mg-8Zn-1.5RE alloy that had been aged for 50 hours at 200 °C is shown in Figure 3. The interdendritic T phase that formed during solidification is indicated as is the B phase that formed during solution treatment at 315 °C.[15,16] The fine precipitates located within the dendrites had formed during aging at 200 °C. This precipitate distribution is shown at higher magnification in Figure 4, where the precipitate morphologies and geometric relationships between precipitates and the α(Mg) matrix are shown more clearly.

The β'_1 precipitates had a rodlike morphology and lay in ($\bar{1}20$) planes of the matrix, with a growth direction of $[001]_{Mg}$. The β'_2 precipitates were disc shaped, lying parallel to the (001) matrix plane. The same types of precipitate formed during aging of all three alloys.

Rare earth elements have very low solubility in Mg solid solution. For example, the maximum solubility of cerium in Mg is about 0.09 at. pct (0.5 wt pct) at 592 °C.[17] EDX/STEM results indicated that in the ternary Mg-Zn-RE alloys investigated here, the rare earth elements were concentrated in the interdendritic Mg-Zn-RE pseudoternary phase (T phase). At the levels of detection possible (0.1 wt pct), no rare earth elements were detected in precipitates dispersed within the dendrites or in the α(Mg) matrix.

D. *Precipitation Sequence*

A series of TEM micrographs taken from the aging sequence for the Mg-8Zn-1.5RE alloy is shown in Figure 5. The foil normal for each specimen was near [010] of the Mg matrix. The precipitate morphologies and dispersions observed in the ternary alloys were very similar to those observed previously in age-hardened Mg-Zn alloys. The microstructure corresponding to the peak hardness after about 20 hours aging indicated that the rodlike β'_1 precipitates were primarily responsible for the age-hardening response. The β'_2 precipitates became extensive at aging times beyond peak hardness.

Plastic deformation occurs mainly by basal slip in these alloys. The interactions between slip dislocations on $(001)_{Mg}$ planes and the β'_1 precipitates can be seen in Figure 6, which was taken from a specimen of the Mg-8Zn-1.5RE alloy after aging 100 hours at 200 °C. The

deformation in this case was introduced by slight bending of the specimen during its preparation. It can be noted that the dislocations bowed between the β'_1 particles as marked by the arrows, and sometimes complex tangles of dislocations, caused by cross slip, arose around the β'_1 particles. This indicates that the rodlike β'_1 precipitates acted as strong pinning points hindering $(001)_{Mg}$ glide, whereas, the large β'_2 disks seemed to provide much less of an obstruction to the movement of these dislocations.

E. *Comparison of Precipitation Behavior between Mg-9Zn and Mg-8Zn-1.5RE*

The precipitate dispersions in Mg-9Zn and Mg-8Zn-1.5RE after aging for 20 and 200 hours at 200 °C can be compared in Figure 7. After 20 hours, the number density of β'_2 disk-shaped precipitates was largest for the binary alloy, indicating that the precipitation sequence had proceeded fastest in this alloy. Substantial coarsening of the β'_2 dispersion accompanied by coarsening and reduction in number of β'_1 precipitates occurred in both alloys after 200 hours at 200 °C.

Measurements of the average diameters of β'_1 and β'_2 precipitates together with the number densities of β'_1 precipitates are given in Table I for both alloys after aging at 200 °C. These measurements were made on TEM micrographs with a $[001]_{Mg}$ beam direction. Each of the quoted diameters is the average of 20 measurements, and the number densities were obtained by counting over at least 4 μm^2 of foil area oriented in an [001] beam direction.

It is clear from these measurements that the rate of coarsening of the β'_1 dispersion in the ternary alloy is considerably less than in the binary alloy, especially for times up to 100 hours. Drastic growth of the β'_2 dispersion occurred in both alloys at 200 hours and coincided with a substantial reduction in the number density of β'_1 precipitates, *i.e.*, β'_2 grew at the expense of β'_1.

Precipitate-free zones formed adjacent to the grain boundaries in both alloys. Preferential precipitation in the grain boundaries during solution treatment depleted the solute in these zones and lead to the absence of precipitates in regions adjacent to the boundaries.

F. *Precipitate Crystal Structures and Orientation Relationships between Precipitates and the Matrix*

Previous work of Sturkey and Clark[6] has pointed out that in Mg-Zn alloys, the β'_1 precipitate is not an equilibrium phase but rather a transition phase that can be designated as MgZn'.[6] The disc-shaped precipitate β'_2 that formed during overaging is the equilibrium phase MgZn. The structure of both precipitates is similar to that of the Laves phase (MgZn$_2$).

The TEM micrographs of rod-shaped β'_1 precipitates and their corresponding SAED pattern with a $[130]_{Mg}$ zone axis are shown in Figure 8. The diffraction streaks from the β'_1 precipitates seemed to contain a number of individual reflections, indicating that the crystal structure of this precipitate may be severely modulated. This is consistent with the β'_1 precipitates being a transition phase.
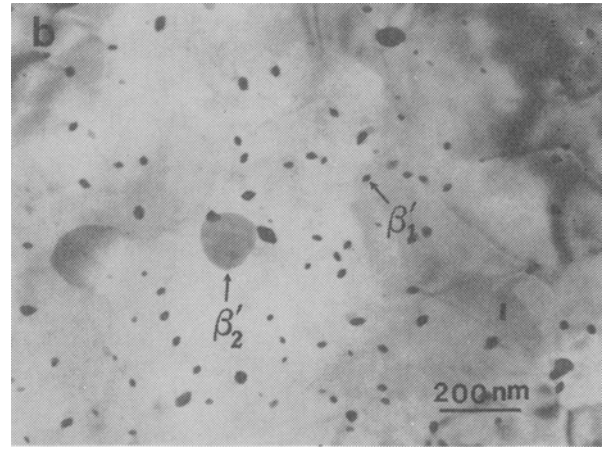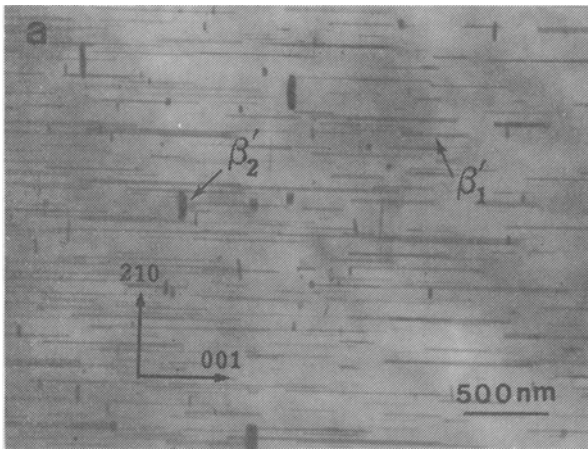
Fig. 4—Precipitation of rod-shaped β_1' and disk-shaped β_2' in Mg-8Zn-1.5RE alloy aged for 20 h at 200 °C (TEM): (a) $[010]_{Mg}$ foil normal and (b) $[001]_{Mg}$ foil normal.
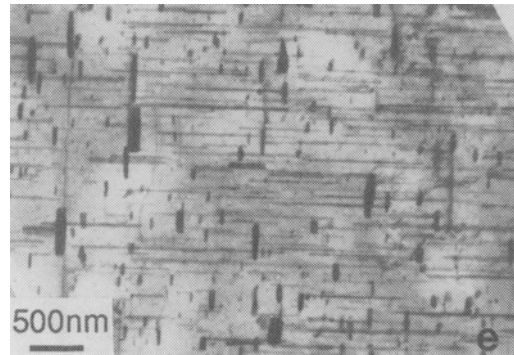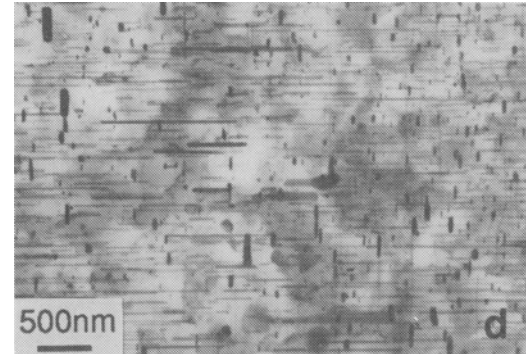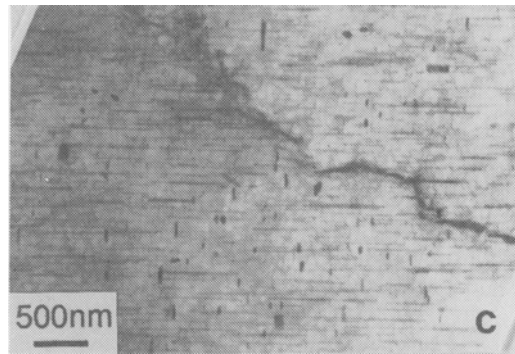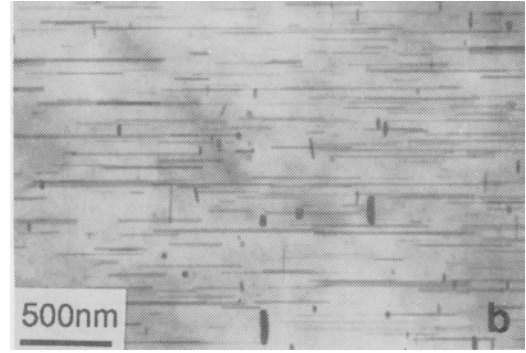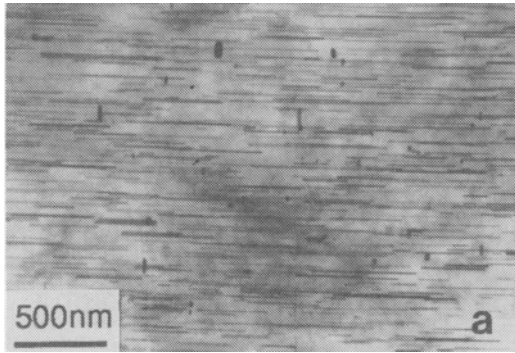
Fig. 5—Aging sequence for the Mg-8Zn-1.5RE alloy (TEM) with foil normals close to $[010]_{Mg}$: (a) 10 h, (b) 20 h, (c) 50 h, (d) 100 h, and (e) 200 h.
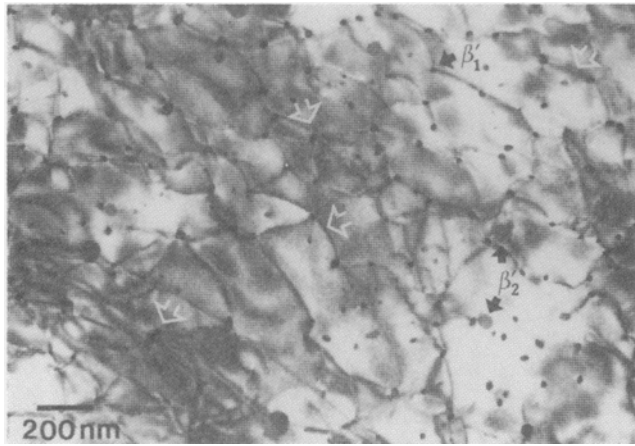
Fig. 6—Interaction of dislocations on (001)Mg with rod-shaped β_1' precipitates in Mg-8Zn-1.5RE alloy aged 100 h at 200 °C (TEM).

Solution of SAED patterns such as that shown in Figure 9 showed that in all three alloys, β_1' obeyed the following orientation relationship with the matrix.[9]

$$[001]_{\beta_1'}//[010]_{Mg} \qquad [110]_{\beta_1'}//[001]_{Mg}$$

The diffraction streaks, which were always perpendicular to the [001] direction of the matrix, passed through the $(00l)_{Mg}$ diffraction spots of the matrix. The overlap of $(110)_{\beta_1'}$ and $(002)_{Mg}$ diffraction spots indicates that the a lattice parameter of the β_1' phase is equal to the c parameter of the Mg matrix; i.e.,

$$a_{\beta_1'} = c_{Mg} = 0.52 \text{ nm}$$

and high coherency between the β_1' phase and matrix can be expected in the $[001]_{Mg}$ direction. Figure 10(a), taken under two beam conditions, reveals the contrast from coherency strain at interfaces between the matrix and β_1' precipitates in a specimen after aging 10 hours at 200 °C. As shown in Figure 10(b), this high degree of coherency strain (arrowed) was maintained for aging times up to 100 hours or more. The size stability of β_1' precipitates and their rodlike morphology are expected to be associated with the close matching between precipitate and matrix crystal lattices.

Electron diffraction showed that the disc-shaped β_2' precipitate had a hexagonal crystal lattice with the lattice parameters $a = 0.525$ nm and $c = 0.855$ nm (the lattice of the matrix was $a = 0.321$ nm and $c = 0.520$ nm). After relatively short aging times, the β_2' precipitate had a small particle size and obeyed the orientation relationship (OR)

$$[00\bar{1}]_{\beta_2'}//[001]_{Mg}; \qquad [120]_{\beta_2'}//[010]_{Mg}$$
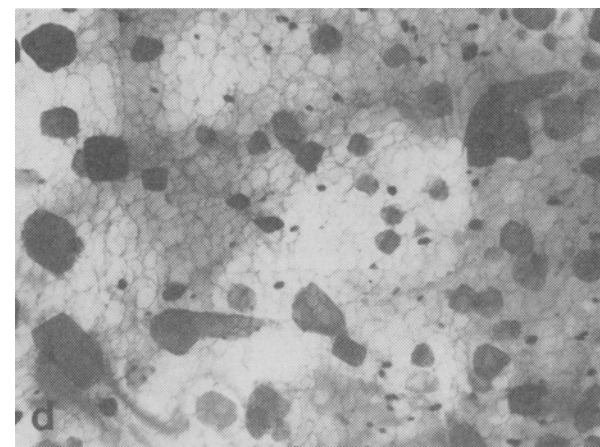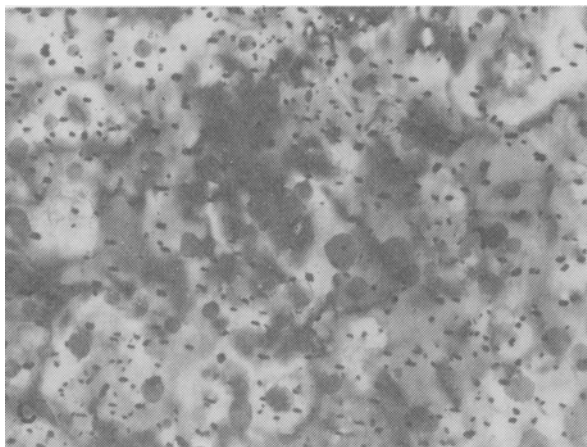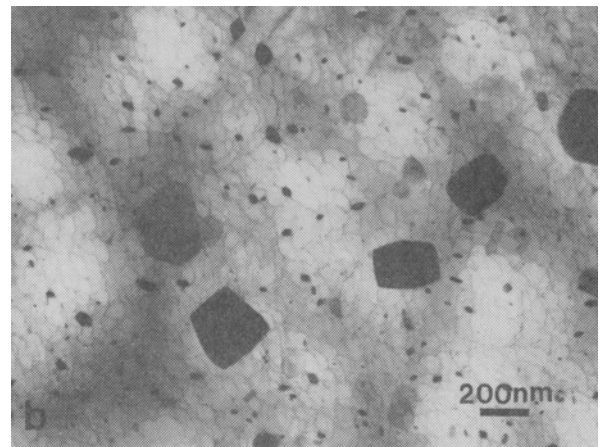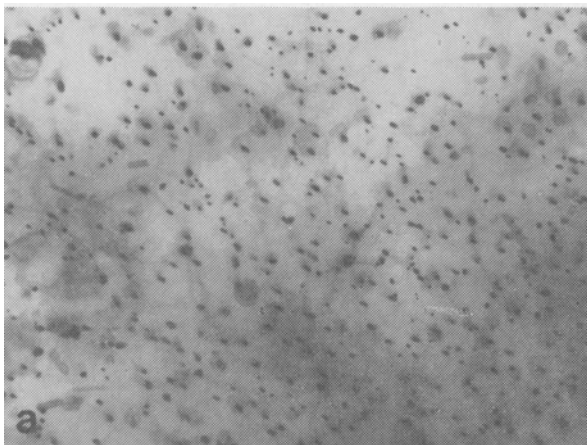
Fig. 7—Comparison of precipitation in Mg-9Zn and Mg-8Zn-1.5RE age hardened at 200 °C: (a) Mg-8Zn-1.5RE, 20 h; (b) Mg-8Zn-1.5RE, 200 h; (c) Mg-9Zn, 20 h; and (d) Mg-9Zn, 200 h.

| Alloy | Aging Time at 200 °C (Hours) | β_1' Rods | | β_2' Disks |
		Average Diameter (nm)	Average Number Density (μm^{-2})	Average Diameter (nm)
Mg-9Zn	20	19	140	82
	100	32	30	90
	200	37	15	162
Mg-8Zn-1.5RE	10	15	180	61
	20	16	184	68
	100	18	94	72
	200	27	33	155
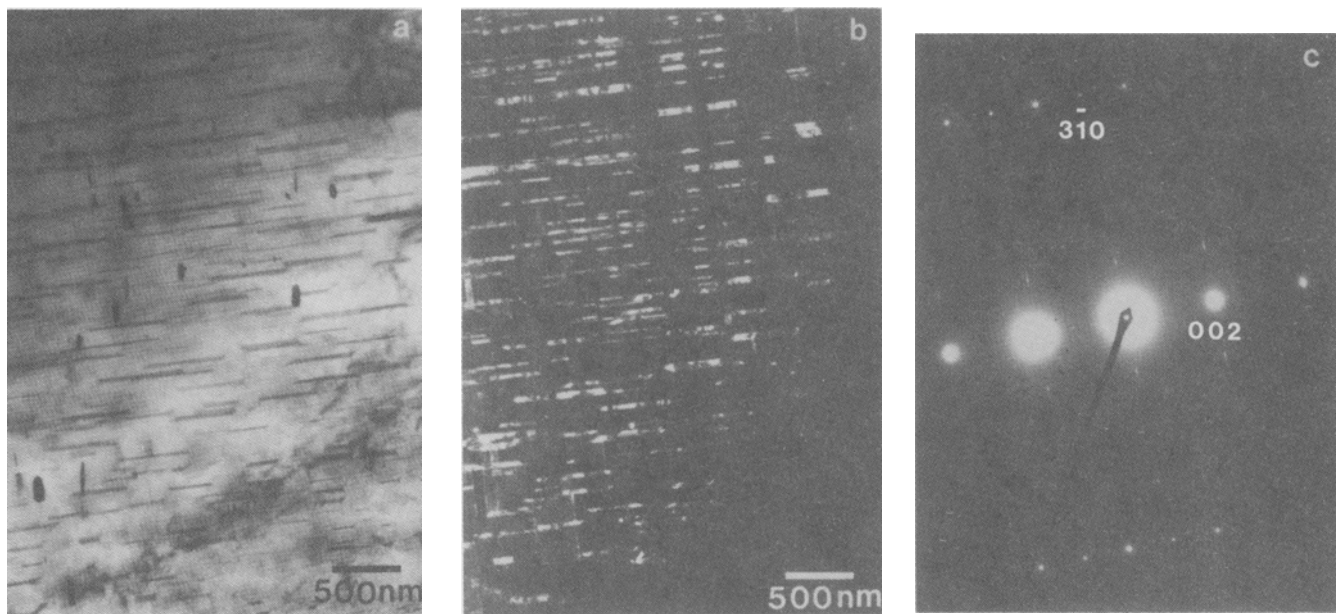
Fig. 8—Precipitation of β_1' and β_2' in Mg-8Zn-1.5RE alloy after 10 h aging at 200 °C (TEM): (a) bright field, (b) dark field formed from concident $(220)_{\beta_1'}$ and weak $(004)_{Mg}$ reflections, and (c) SAED pattern [130] matrix zone.

which is the same result as that obtained using X-ray diffraction on binary Mg-Zn alloys.[8] The TEM images and SAED pattern shown in Figure 11 were taken from a specimen aged for 10 hours at 200 °C. The dark-field image indicates that most of the β_2' particles, except the very large one (arrowed), obeyed the OR mentioned previously.

In general, four different ORs were found for β_2' in specimens that had been aged for times longer than 10 hours. In all four relationships, the basal plane of β_2' is parallel to the basal plane of the matrix, but each relationship has a different angle of rotation around the $[001]_{Mg}$ direction. These multiple ORs became pronounced upon overaging. Figure 12(a) is a TEM micrograph taken from a specimen aged for 100 hours at 200 °C and in a region close to a large intergranular particle. The relevant diffraction patterns shown in Figures 13(a) and (b) were taken with $[130]_{Mg}$ and $[140]_{Mg}$ zone axes of the matrix, respectively. Reflections from

four orientation variants of β_2 precipitates could be distinguished. The streaked reflections in the diffraction patterns in Figures 13(a) and (b) came from β_1' precipitates that coexisted with β_2'. The corresponding dark-field images for each variant of β_2' precipitate are shown in Figures 12(b) through (d). The ORs between β_2' and matrix, as listed subsequently, were deduced from a series of diffraction patterns including those in Figure 13.

$$[00\bar{1}]_{\beta_2'}//[001]_{Mg} \quad [010]_{\beta_2'}//[120]_{Mg}$$

$$[00\bar{1}]_{\beta_2'}//[001]_{Mg} \quad [140]_{\beta_2'}//[130]_{Mg}$$

$$[00\bar{1}]_{\beta_2'}//[001]_{Mg} \quad [150]_{\beta_2'}//[140]_{Mg}$$

$$[00\bar{1}]_{\beta_2'}//[001]_{Mg} \quad [010]_{\beta_2'}//[130]_{Mg}$$

The first of these relationships is the same as that reported by Gallot and Graf.[8]

- • matrix 010 zone axis
- ○ β_1' 001 zone axis
- □ β_2' 210 zone axis
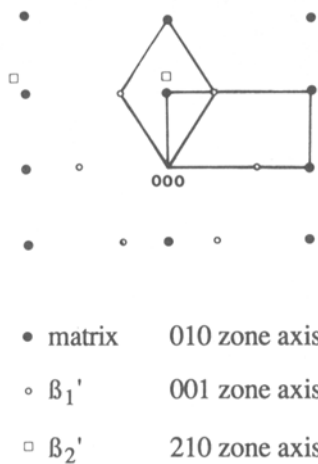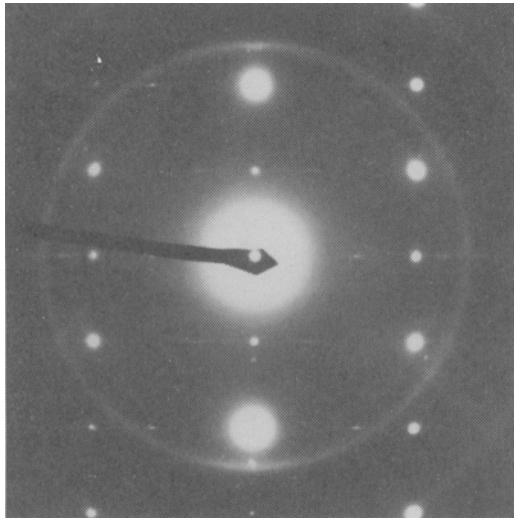
Fig. 9—SAED pattern from $[010]_{Mg}$ zone axis and its schematic solution showing the OR between β_1' and the Mg matrix to be $[001]_{\beta_1'}//$ $[010]_{Mg}$; $[1\bar{1}0]_{\beta_1'}//[001]_{Mg}$.

IV. DISCUSSION

A. Precipitation Reactions during Age Hardening

It is clear from comparison of the age-hardening curves (Figure 2) with TEM micrographs of the precipitate dispersions (Figure 5) that peak hardness during aging of these alloys is due to formation of a fine scale dispersion of rod-shaped β_1' precipitates. These precipitates lie in a $[001]_{Mg}$ direction and effectively pin dislocations moving on $(001)_{Mg}$ planes (Figure 6). The density of the β_1' precipitate dispersion thus determines the hardness of the age-hardened alloys.

Overaging is caused by transformation of the β_1' precipitate dispersion to a dispersion of disk-shaped β_2' precipitates that lie on $(001)_{Mg}$ planes. Since these β_2' precipitates do not penetrate many $(001)_{Mg}$ planes, they are easily bypassed by dislocations and make a poor contribution to the resistance to plastic flow. The β_2' precipitate dispersion forms by transformation from the β_1' precipitate dispersion, and therefore, delay of this transformation is important for improving the resistance of alloys of this type to overaging.
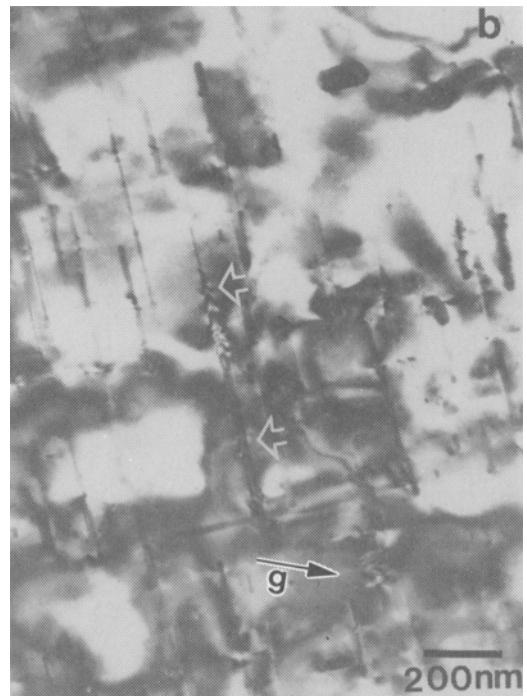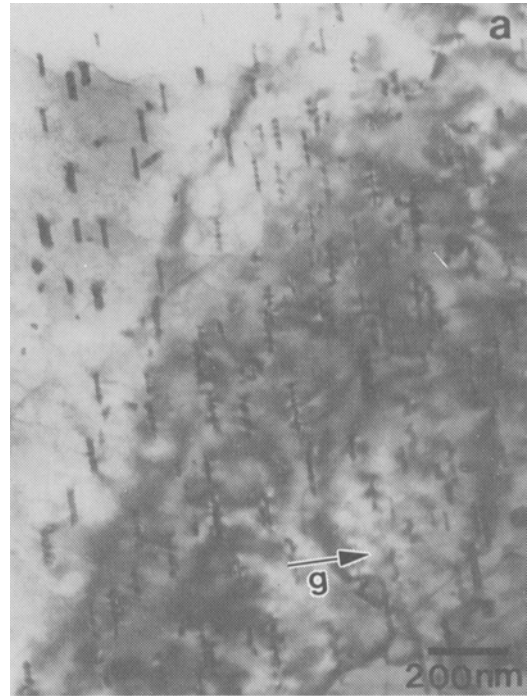
Fig. 10—Coherency strains at the interfaces between β_1' rods and the Mg matrix. Mg-8Zn-1.5RE, TEM bright field, two beam diffraction conditions: (a) after aging 10 h, $g = (110)_{Mg}$; and (b) after aging 100 h, $g = (101)_{Mg}$.

B. The Influence of Rare Earth Additions on Age Hardening of Mg-Zn-RE Alloys

Although no rare earth elements were detected in the solution-treated matrix or in the precipitates, it seems that these minor elements might play an important role in the age-hardening response of Mg-Zn-RE alloys. Comparison of macro- and microhardness measurements
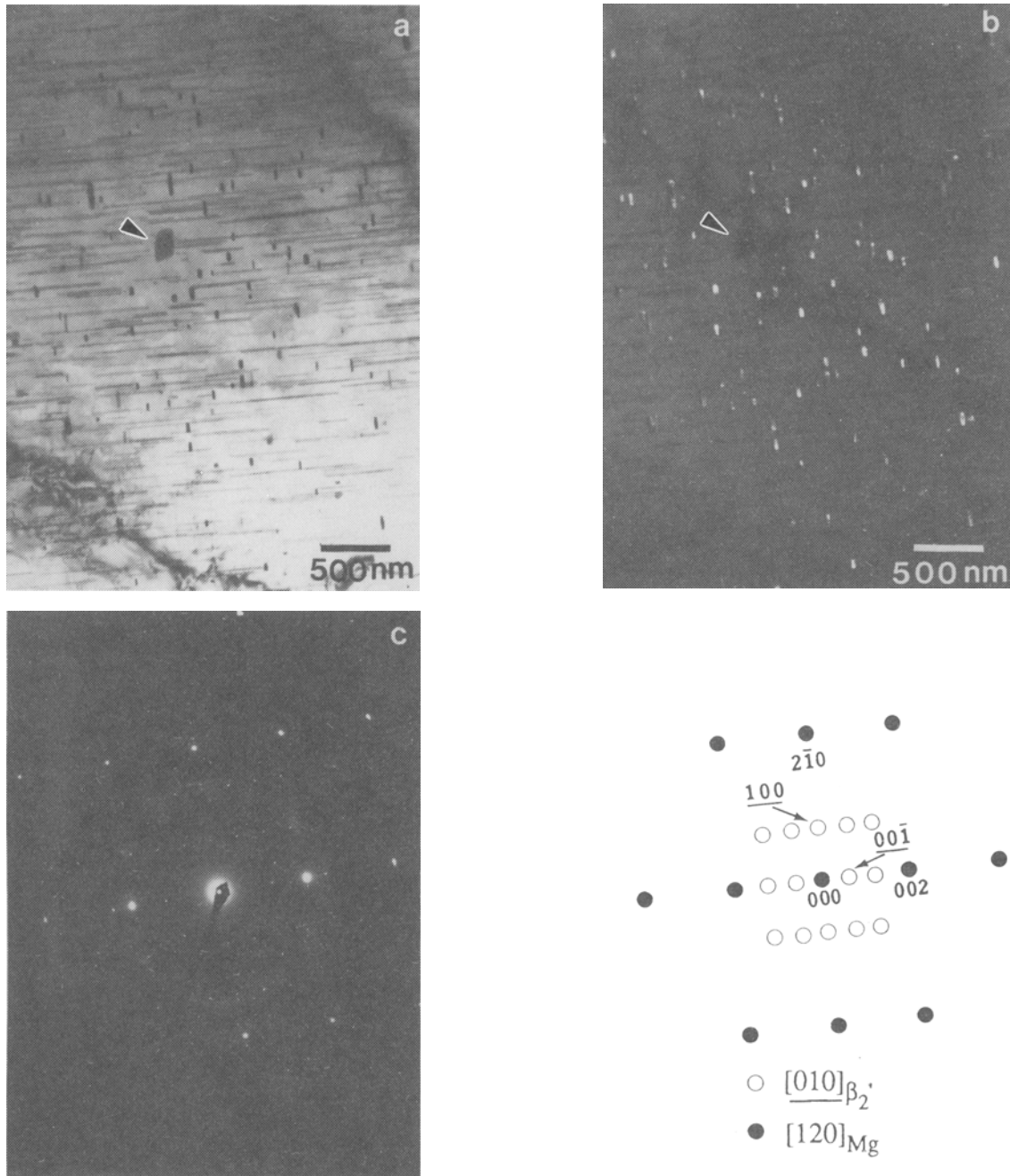
Fig. 11 — Early precipitation of β'_2 in Mg-8Zn-1.5RE alloy after aging 10 h at 200 °C. (a) Bright field, taken with $[120]_{Mg}//[010]_{\beta'_2}$ beam direction. (b) Dark field of β'_2 precipitate dispersion. (c) SAED pattern with $[120]_{Mg}/[010]_{\beta'_2}$ zone axis showing the OR $[00\bar{1}]_{\beta'_2}//[001]_{Mg}$; $[120]_{\beta'_2}//[010]_{Mg}$.

from age-hardened specimens of Mg-9Zn and Mg-8Zn-1.5RE alloys indicates that the rare earth additions decrease the rate of age hardening and decelerate overaging. It can be seen from Figure 7 that the rare earth additions retarded the nucleation of β'_2 precipitates and consequently delayed the decrease in the number of the β'_1 precipitates during overaging.

Measurements of the average diameters of β'_2 disks (Table I) revealed little difference in the growth rate of β'_2 particles between aged specimens of Mg-9Zn and Mg-8Zn-1.5RE alloys. However, the larger number of β'_2 precipitates in the Mg-9Zn alloy led to more rapid ex-

haustion of the β'_1 precipitate dispersion than in the Mg-8Zn-1.5RE alloy. Thus, the rare earth containing alloy was more resistant to overaging than the Mg-9Zn alloy.

C. *The Orientation Relationship between β'_1 Precipitates and the Matrix*

The β'_1 precipitates have a rodlike shape with an axis parallel to $[001]_{Mg}$, because the lattice parameters of the two phases are virtually equal in this direction; *i.e.*,

$$a_{\beta'_1} = c_{Mg} = 0.52 \text{ nm}$$
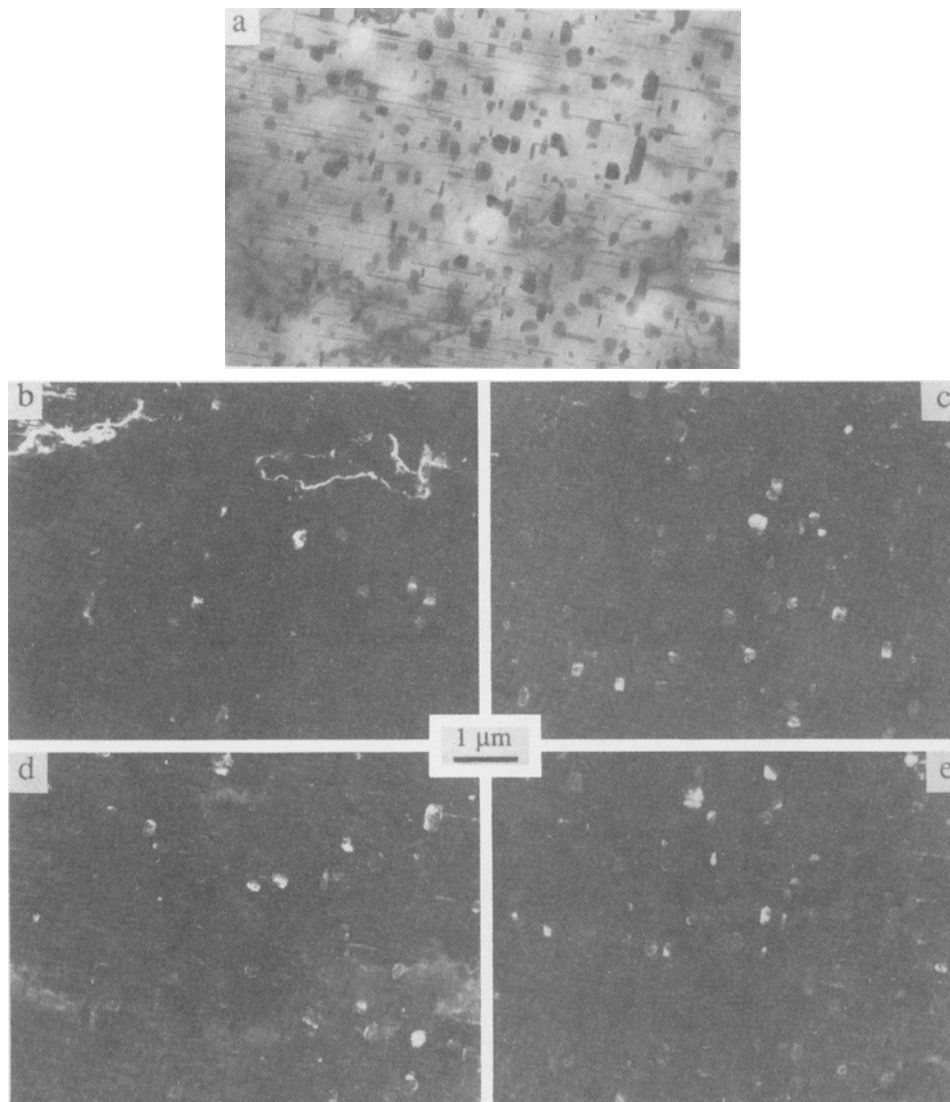
Fig. 12—β_2' precipitate dispersion in Mg-8Zn-1.5RE alloy after aging for 100 h at 200 °C, showing four different ORs with the matrix: (a) bright field, $[130]_{Mg}$ beam direction; (b) dark field of $[\beta_2']_1$, $[130]_{Mg}$ beam direction; (c) dark field of $[\beta_2']_2$, $[140]_{Mg}$ beam direction; (d) dark field of $[\beta_2']_3$, $[140]_{Mg}$ beam direction; and (e) dark field of $[\beta_2']_4$, $[130]_{Mg}$ beam direction.

This leads to a high degree of coherency between matrix and precipitate at their circumferential interface. The precipitates develop a rodlike shape because this low energy interface is favored, and the rate of thickening of the precipitates is very low because this would involve the climb of complex interfacial misfit dislocations.

Thus, because of the low degree of mismatch between a_{β_1} and c_{Mg}, the precipitates adopt the $[001]_{\beta_1}//[010]_{Mg}$, $[1\overline{1}0]_{\beta_1}//[001]_{Mg}$ OR with a needlelike shape. Their orientation with long axis parallel to $[001]_{Mg}$ is ideal for the provision of barriers to dislocation slip on $(001)_{Mg}$ planes.

D. *An Interpretation of the Orientation Relationships between β_2' Precipitates and the Matrix*

The energy of an interphase boundary depends on many parameters, with atomic interaction energy and elastic energy due to interfacial misfits being two of the most important factors to be taken into account. The near-CSL (coincident site lattice) model can be used to describe

the equilibrium structure of coherent and semicoherent boundaries and relevant ORs.[18,19,20] The only general rule seems to be that the favored orientations correspond to a relatively dense CSL. Deviation from a high-density CSL orientation to relax and decrease the whole energy of the system occurs by formation of an equilibrium structure in the phase boundary. The final interfacial structure consists of grain boundary dislocation (GBD) networks embedded in the high-density CSL boundary. The Burgers vectors of the GBD networks are generally vectors of the DSC lattice, defined by Bollmann,[18] that correspond to the high-density CSL.

In the hexagonal Mg-Zn and Mg-Zn-RE alloys, the basal planes of β_2' precipitates in all four orientation relationships (OR) are parallel to the basal plane of the matrix. However, they have different angles of rotation around the [001] direction. Therefore, for these four kinds of OR, the interphase boundaries parallel to $(001)_{Mg}$, which is the habit plane of β_2' precipitates, are formed between planes that have the same hexagonal lattice patterns in
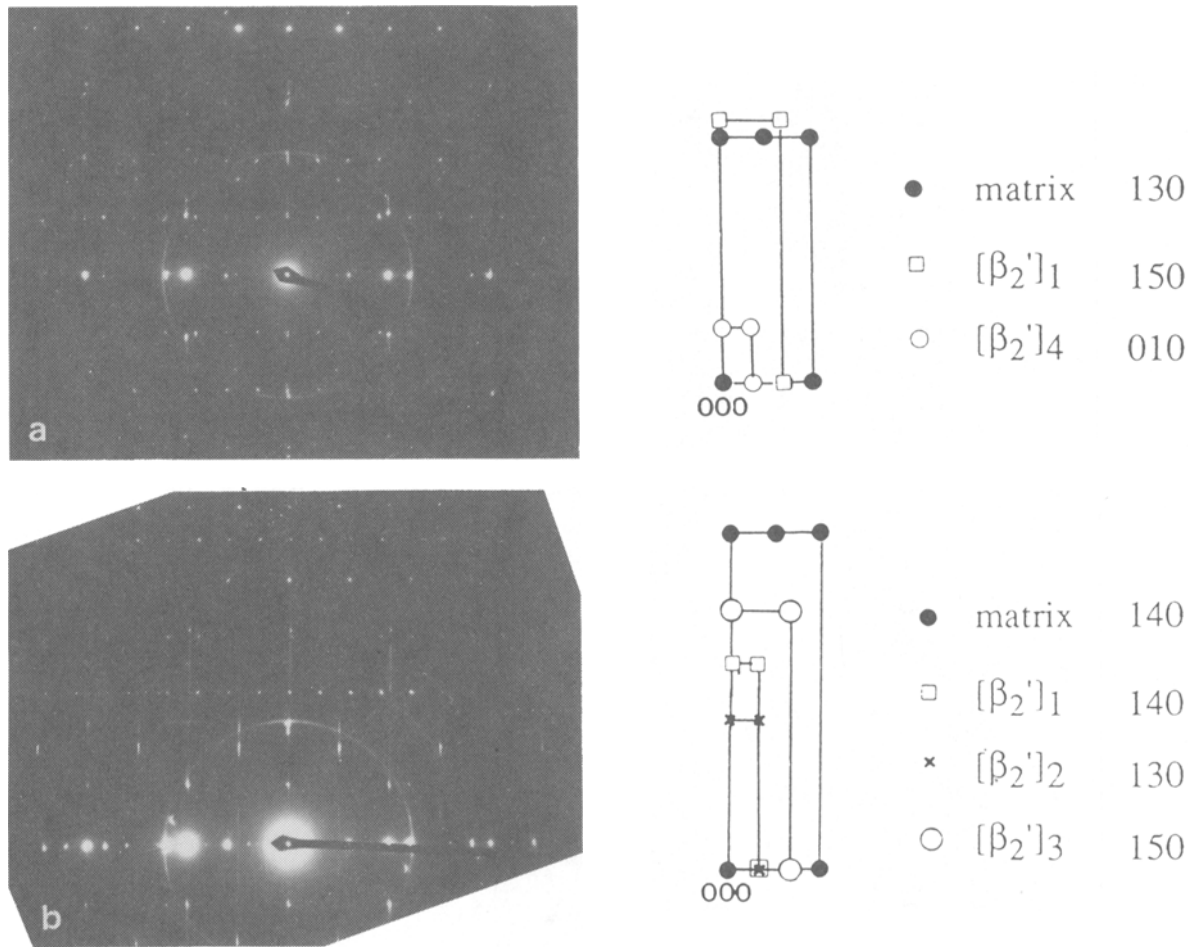
Fig. 13 — ORs between β_2' and matrix in Mg-8Zn-1.5RE alloy aged for 100 h at 200 °C. (*a*) SAED with $[130]_{Mg}$ zone axis showing the ORs between $[\beta_2']_1$, $[\beta_2']_4$, and the matrix. (*b*) SAED with $[140]_{Mg}$ zone axis showing the ORs between $[\beta_2']_1$, $[\beta_2']_2$, $[\beta_2']_3$, and the matrix.

each crystal. However, the size of these patterns is different. Such boundaries may be characterized as "hexagon-on-hexagon." The lattice parameters for the two phases were determined by TEM to be $a_{Mg} = 0.321$ nm, $c_{Mg} = 0.520$ nm and $a_{\beta_2'} = 0.525$ nm, $c_{\beta_2'} = 0.855$ nm. In the [001] direction, near-CSL sites can be chosen at positions close to $3c_{\beta_2'}$ and $5c_{Mg}$ for all ORs, and the mismatch of the two lattices at these near-coincidence sites is $\delta = -1.35$ pct. It is then just necessary to take the two-dimensional near-CSL on (001) planes into account.

Four near-coincidence positions can be obtained by rotation of the β_2' lattice with respect to that of the matrix about the $[001]_{Mg}/[001]_{\beta_2'}$ direction, which is the normal to the two basal planes. These positions (Figures 14(a) through (d)) correspond to the four ORs between β_2' and the Mg matrix that were found in this investigation. Each of the hexagon-shaped planar near-CSL, marked with the lattice vector $\mathbf{a}_{CSL}$ in Figure 14, form an interpenetrating crystal structure that can be characterized by the mismatch parameter δ, given by

$$\delta = 2(r_p - r_m)/r_p + r_m$$

where r_p and r_m are the respective precipitate and matrix lattice vectors of the two matching cells in the boundary

plane. The term Σ is the number of lattice sites of each phase in a unit cell of a near-CSL and it is a measure of the size of the near-CSL. The values of the mismatch δ and $\Sigma_{\beta_2'}/\Sigma_{Mg}$ for all four ORs are given in Table II.

For short aging times (20 hours or less), virtually all of the β_2' precipitates present in the alloys obeyed OR 1; *i.e.*,

$$[00\bar{1}]_{\beta_2'}//[001]_{Mg}; \qquad [010]_{\beta_2'}//[120]_{Mg}$$

For this OR, Σ_{Mg} and $\Sigma_{\beta_2'}$ are low ($\Sigma_{Mg} = 3$ and $\Sigma_{\beta_2'} = 1$) but the lattice misfits at the near-coincident sites are large ($\delta = -5.7$ pct). Thus, the boundary structure needs to be relaxed by introduction of a regular array of GBDs in order to obtain a structure with minimum energy. The Burgers vectors of these GBDs should be equal to the lattice vectors of the DSC. The DSC lattice for OR 1 is drawn in Figure 14(a) according to Grimmer's theory.[21] The Burgers vectors of perfect GBDs are the translation vectors of the DSC lattice, which for this case, are close to $b_1 = [1/3 \ 2/3 \ 0]_{Mg}$, $b_2 = [2/3 \ 1/3 \ 0]_{Mg}$. These edge dislocations, which are normal to the $(001)_{Mg}$ plane, occur at intervals of about 3.3 nm. The interface can be regarded as a semicoherent boundary.

The dense secondary dislocation networks embedded in the interfacial plane can be expected to restrict growth
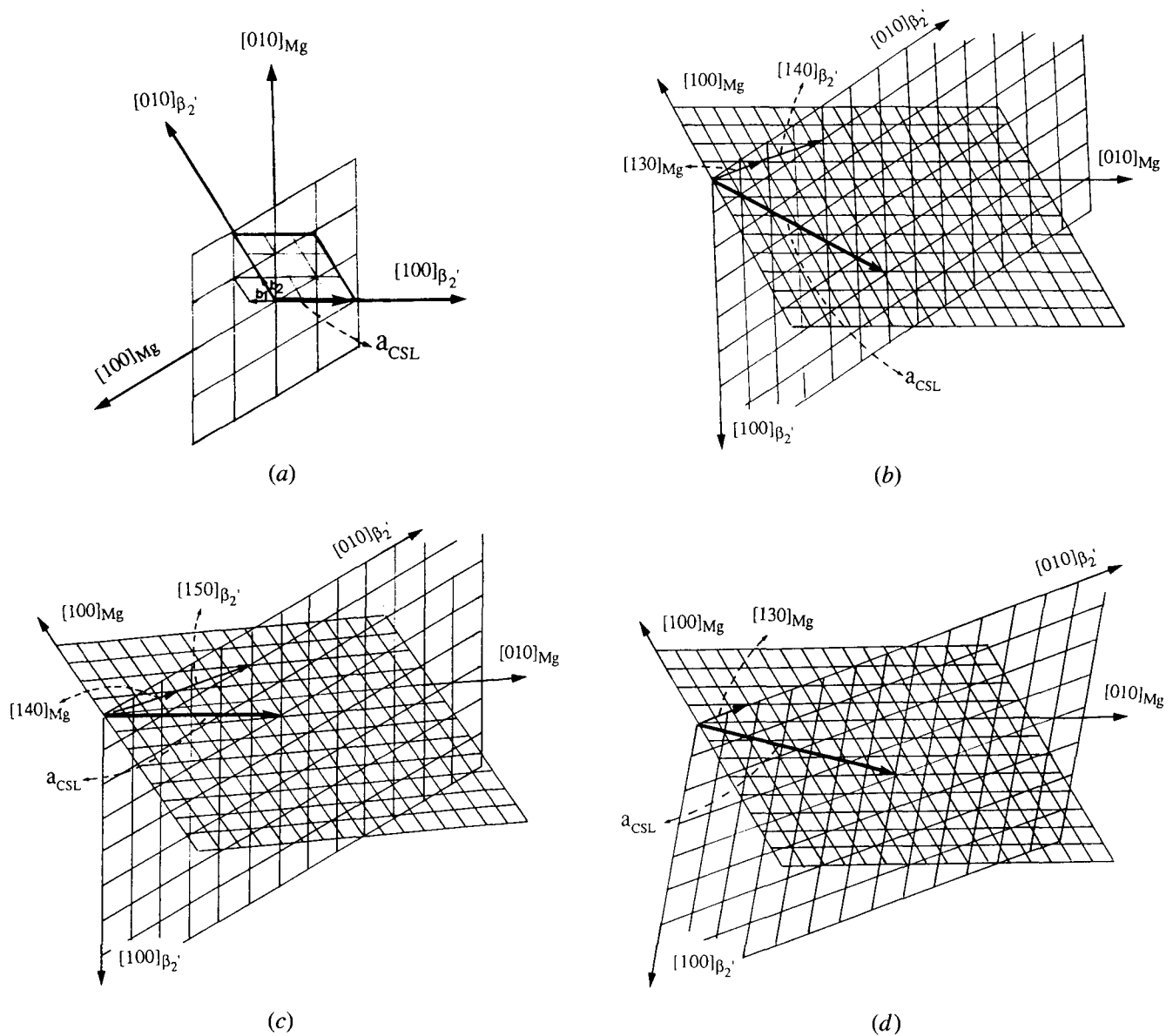
Fig. 14—Schematic diagrams of $(001)_{Mg}//(001)_{\beta_2'}$ planes in interpenetrating β_2' and Mg crystal lattices: (a) OR 1, (b) OR 2, (c) OR 3, and (d) OR 4.

Table II. $\Sigma_{\beta_2'}/\Sigma_{Mg}$ for the Near-CSLs and the Mismatch δ of Lattice Vectors of Near-Coincidence Sites for the Four Orientation Relationships on $(001)_{Mg}//(00\bar{1})_{\beta_2'}$

Orientation Relationship on $(001)_{Mg}//(00\bar{1})_{\beta_2'}$	Lattice Vectors of Near-CSL in		$\Sigma_{\beta_2'}/\Sigma_{Mg}$	Mismatch δ (Pct)
	β_2'	Mg		
$[010]_{\beta_2'}//[120]_{Mg}$	$[010]]_{\beta_2'}$	$[120]_{Mg}$	1/3	−5.7
$[140]_{\beta_2'}//[130]_{Mg}$	$6[110]]_{\beta_2'}$	$[560]_{Mg}$	39/91	2.8
$[150]_{\beta_2'}//[140]_{Mg}$	$3[120]]_{\beta_2'}$	$[180]_{Mg}$	27/73	0.27
$[010]_{\beta_2'}//[130]_{Mg}$	$[470]]_{\beta_2'}$	$[380]_{Mg}$	37/97	−0.5

perpendicular to this plane, since this would require co-operative climb of the dislocations in the boundary. Broadening of the planar disks is also restricted, since this would require more energy associated with the development of dislocation networks. It is therefore not surprising that OR 1 predominated in specimens aged for a short time, where the β_2' precipitates were small.

For specimens aged for longer times, the other three ORs occurred in association with marked coarsening of the disc-shaped β_2' particles. The values in Table II indicate that rotation of the $(001)_{\beta_2'}$ plane with respect to $(001)_{Mg}$ can decrease the degree of mismatch δ and relax the elastic strain energy. As indicated by the much higher Σ values, the degree of coherency for ORs 2 through 4 are much lower than for OR 1. Therefore, the interfacial energy for the particles obeying these ORs increased a certain degree. However, the elastic strain energy decreased by relaxation of the boundary structure.

V. CONCLUSIONS

1. Both Mg-Zn and Mg-Zn-RE alloys age harden by precipitation of rod-shaped β_1' precipitates.
2. Overaging is due to the transformation of the β_1' precipitate dispersion to a dispersion of disc-shaped β_2' precipitates.
3. The β_1' precipitates obey a crystallographic OR with the matrix that was first reported by Gallot et al.[9]
4. The β_2' precipitates exhibit four different crystallographic ORs with the matrix. In all four relationships, the basal planes of precipitate and matrix are parallel but the lattices are rotated different amounts about $[001]_{Mg}$.
5. The ORs between the β_2' precipitates and the matrix can be explained by the near-CSL model.
6. Precipitation of β_2', and thus the onset of overaging, is delayed by rare earth additions.

REFERENCES

1. J.B. Clark and F.N. Rhines: *J. Met.*, 1957, vol. 209, pp. 425-30.
2. Nair K. Suseelan and M.C. Mittal: *Mater. Sci. Forum*, 1988, vol. 30, pp. 89-103.
3. M.J. Miles: *Pres. Ann. Nat. For. Amer. Helicopter Soc.*, Washington, D.C., May, 1977.
4. B. Lagowski: *AFS Trans.*, 1977, vol. 85, pp. 237-40.
5. *Metals Handbook* 9th ed., ASM INTERNATIONAL, Metals Park, OH, 1979, vol. 2, pp. 526 and 579.
6. L. Sturkey and J.B. Clark: *J. Inst. Met.*, 1959–60, vol. 88, pp. 177-81.
7. J.B. Clark: *Acta Metall.*, 1965, vol. 13, pp. 1281-89.
8. J. Gallot and R. Graf: *Comptes Rendu*, 1965, vol. 261B, pp. 728-31.
9. J. Gallot, K. Lal, R. Graf, and A. Guinier: *Comptes Rendu*, 1965, vol. 258B, pp. 2818-20.
10. E.O. Hall: *J. Inst. Met.*, 1968, vol. 96, pp. 21-27.
11. G. Mima and Y. Tanaka: *Trans. Jpn. Inst. Met.*, 1971, vol. 12, pp. 71-75.
12. G. Mima and Y. Tanaka: *Trans. Jpn. Inst. Met.*, 1971, vol. 12, pp. 76-81.
13. G. Mima and Y. Tanaka: *Trans. Jpn. Inst. Met.*, 1971, vol. 12, pp. 317-22.
14. G. Mima and Y. Tanaka: *Trans. Jpn. Inst. Met.*, 1971, vol. 12, pp. 323-28.
15. L.Y. Wei, G.L. Dunlop, and H. Westengen: Luleå University of Technology, Luleå, Sweden, unpublished research, 1993.
16. L.Y. Wei and G.L. Dunlop: *New Materials and Processes*, Proc. 5th SSMS, I.L.H. Hansson and H. Liholt, eds., Danish Society for Materials Testing and Research, The House of Engineers, Copenhagen, 1989, pp. 721-28.
17. A.A. Nayeb-Hashemi and J.B. Clark: *Bull. Alloy Phase Diagrams*, 1988, vol. 9 (2), pp. 162-72.
18. W. Bollmann: *Crystal Defects and Crystalline Interfaces*, Springer, Berlin, 1970, pp. 143-228.
19. R.W. Balluffi, A. Brokman, and A.H. King: *Acta Metall.*, 1982, vol. 30, pp. 1453-70.
20. R. Wang and G.L. Dunlop: *Acta Metall.*, 1984, vol. 32, pp. 1591-99.
21. H. Grimmer: *Scripta Metall.*, 1974, vol. 8, pp. 1221-23.